10

Super Resolved Holographic Configurations

Amihai Meiri[1], Eran Gur[2], Javier Garcia[3], Vicente Micó[3], Bahram Javidi[4] and Zeev Zalevsky[1]

[1]*Faculty of Engineering, Bar-Ilan University, Israel*
[2]*Department of Electrical Engineering and Electronics, Azrieli – College of Engineering, Israel*
[3]*Departamento de Óptica, Universitat Valencia, Spain*
[4]*Department of Electrical and Computer Engineering, University of Connecticut, USA*

10.1 Introduction

Optical imaging suffers from a drawback inherent to the process of recording: the recording media (either photographic film or a digital camera) captures only the intensity of the incident light, sacrificing the three-dimensional data in the process, which lies in the phase of the electric field. In 1948 Dennis Gabor invented a technique which circumvents the loss of phase by adding a reference field to the recorded object [1]. This technique is dubbed *holography*, where the interference patterns between the object and the reference field can be recorded. These interference fringes depend on the phase of the object, therefore maintaining this information. If we write the recorded object in terms of amplitude and phase, $a = |a|e^{j\phi}$ add a reference field A and record the obtained intensity we have

$$||a|e^{j\phi} + A|^2 = |a|^2 + |A|^2 + aA\cos\phi \tag{10.1}$$

The first term is the intensity of the recorded field as in a conventional imaging system and the second term is the intensity of the reference field. The last term reveals that the phase information is maintained and recorded on the imaging medium as well.

Multi-dimensional Imaging, First Edition. Edited by Bahram Javidi, Enrique Tajahuerce and Pedro Andrés.

As in every imaging system, holography is limited in both resolution and field of view (FOV). Another drawback in this technique is the excess information: the intensity of the reference beam (the second term in Eq. (10.1)) and the so-called twin image problem which is explained in the next section. Both factors deteriorate the quality of the hologram.

In this chapter we show how metal nanoparticles come to the aid of holography in improving the resolution, FOV, and eliminating the twin image and reference field.

10.2 Digital Holography

The original holography scheme, suggested by Dennis Gabor, is presented in Fig. 10.1. In the Gabor hologram the object is assumed to be highly transmissive, with transmission function

$$T(x,t) = T + \Delta T(x,y), \tag{10.2}$$

where T is the average transmission and $\Delta T(x,y)$ is the variation in space. The high transmissivity of the object means that $\Delta T << T$. In this configuration, T serves as the reference beam. Looking as before at the scattered object beam a and the reference beam A we can write the recorded intensity as

$$I = |A+a|^2 = |A|^2 + |a|^2 + A^*a + Aa^*. \tag{10.3}$$

If we illuminate the developed recording medium I by a reference beam A', the result is $I' = A'I$. Note that, in writing both the recorded intensity and the reconstructed intensity, we assumed that the amplitude transmittance of the developed hologram is proportional to the exposure, and for simplicity of argument it is assumed that this proportionality constant is 1. The generalization of the theory in that case is straightforward [2]. Looking at the four terms of Eq. (10.3) we can neglect the second term due to our assumption about the transmissivity of the object. We are left with three terms: the first term of Eq. (10.3) that is the reference beam, the third term of Eq. (10.3) that is our desired field multiplied by a constant, and the last term of Eq. (10.3) that is the complex conjugate of the field, termed the *twin image*. The reference beam and the twin image deteriorate the quality of the hologram and are a major drawback of the on-axis hologram.

To solve the DC term (reference wave) and twin image problem Leith and Hupetnieks [3] suggested using an off-axis setup, where the reference is incident on the recording medium at

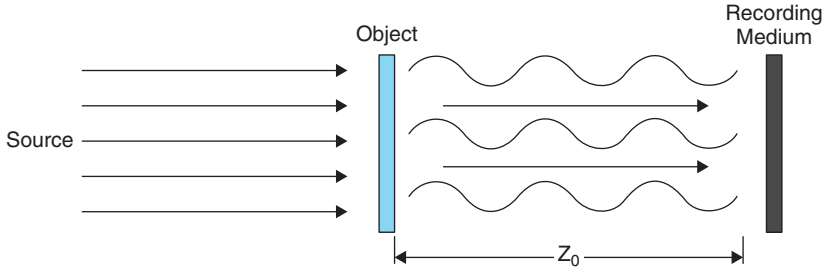

Figure 10.1 Gabor hologram. *Source*: Amihai Meiri, Eran Gur, Javier Garcia, Vicente Micó, Bahram Javidi, Zeev Zalevsky 2013. Reproduced with permission from SPIE

an angle: $Ae^{-j2\pi \sin 2\theta x/\lambda}$, where θ is the angle between the reference beam and the optical axis. The recorded hologram in this case is

$$I = \left|a + Ae^{-j2\pi \sin 2\theta x/\lambda}\right|^2 = |A|^2 + |a|^2 + A^* e^{j2\pi \sin 2\theta x/\lambda} a + Ae^{-j2\pi \sin 2\theta x/\lambda} a^*. \tag{10.4}$$

The phase factors of the last two terms translate into spatial shift as a result of the free space propagation. Now we have two on axis fields – the intensity of the object and the reference beam, and two off axis – the last two terms, one above the optical axis and one below it. This enables us to spatially filter out the unwanted terms. The information bandwidth captured by this solution is smaller than the on-axis hologram.

Since all the information is present in the recorded hologram, a digitally recorded hologram does not need a reconstruction method, but the information can be digitally analyzed. As an example to such a procedure we can look at the focusing of the hologram. In presenting the basic theory of holography we neglected the axial position of the hologram. Looking at a point source in the reference beam location, the object source location, and the reconstruction source location, we can show that the object beam results in a virtual image positioned at a distance of Z_0 before the recording medium and a twin image being a real image formed at a distance of Z_0, behind the recording medium [2]. Assuming that the distance Z_0 is relatively large, we look at the unfocused recorded hologram. By digitally implementing a Fresnel diffraction integral we can propagate the recorded hologram by a distance of $-Z_0$ and obtain the focused virtual image. Now the real image (the twin image) is highly unfocused and its influence on the quality of the recorded hologram is relatively small. In the case of microscopy, where the distances are small, such a solution is inadequate and the twin image must be eliminated by other means, such as phase retrieval [4], deconvolution [5], and recording of multiple holograms in different axial locations [6].

10.3 Metal Nanoparticles

Owing to their various size, shapes and materials, metal nanoparticles became a major interest, especially in the fields of imaging and biomedical engineering. Their attractiveness stems from the sensitivity of their absorption and scattering spectrum to these attributes [7,8]. This sensitivity is explained by the oscillation of electrons in the conduction bend as a result of an incident electric field. When these electrons oscillate coherently the absorption and scattering are at their peak and a distinct resonance can be observed [9]. This phenomenon is known as *surface plasmon resonance* (SPR).

The simplest of shapes for these nanoparticles is a sphere (see Fig. 10.2). Looking at gold (Au) spheres, their apparent color is red, where the exact shade depends on the size of the nanoparticles. An example of SPR can be seen in Fig. 10.3, where the absorption spectra of variously sized nanospheres are presented.

The sensitivity of the extinction spectrum of metal nanoparticles is not limited to their size. Their shape is also an important factor. Nanorods, cigar shaped nanoparticles, exhibit different spectra to nanospheres where the peak is red-shifted. In addition, their aspect ratio, the ratio between their length and diameter, also determines the location of the extinction peak [10]. Other factors that determine their spectrum are the surrounding medium's refractive index [11], the material from which the nanoparticles are made [7], and their density due to inter-particle coupling [12,13].

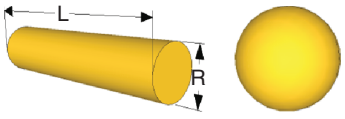

Figure 10.2 Metal nanoparticles are fabricated in various shapes. *Left* – a nanorod with an aspect ratio of L/R. *Right* – a nanoshpere. *Source*: Amihai Meiri, Eran Gur, Javier Garcia, Vicente Micó, Bahram Javidi, Zeev Zalevsky 2013. Reproduced with permission from SPIE

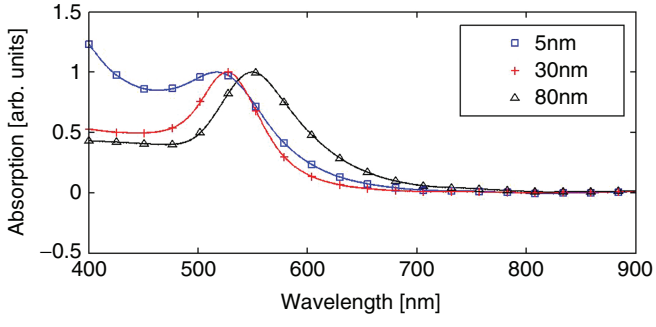

Figure 10.3 Measured spectra of various gold nanospheres. *Source*: Amihai Meiri, Eran Gur, Javier Garcia, Vicente Micó, Bahram Javidi, Zeev Zalevsky 2013. Reproduced with permission from SPIE

Metal nanoparticles are attractive not only due to SPR. They also exhibit a high scattering cross section, which reduces the image acquisition time and high stability [14], all in comparison to fluorescent markers, which are in common use in various imaging systems [15,16].

Usually metal nanoparticles are suspended in liquid and due to their small size they move in Brownian motion. The Brownian motion was used by Gur *et al.* [17] as a random encoding mask for super-resolved microscopy, a technique that is the foundation of the methods presented in this chapter. This technique is presented briefly here.

When metal nanoparticles are suspended in liquid and are placed close to a high resolution object, their location constantly changes. Each metal nanoparticle couples the non-propagating near field to a propagating field that can be recorded by a camera. Since the near field is not diffraction limited, its resolution is not limited, but by the size of the nanoparticles in a manner that resembles apertureless *Near field Scanning Optical Microscope* (aNSOM) [18]. If we denote the high resolution object by $s(x)$, the time varying random nanoparticles mask by $g(x,t)$, and the point spread function (PSF) of the optical system by $p(x)$, each frame that is captured by the camera can be written as

$$I(x,t) = \int s(x')g(x',t)p(x-x')dx'. \tag{10.5}$$

When multiple frames are recorded, over time, the nanoparticles cover the entire area of the object to be imaged. Due to their small size, each nanoparticle can be considered as a point source and therefore, on the recording medium it has a shape of a PSF. When these nanoparticles are sparse enough (a distance of at least half a wavelength is required), each of these nanoparticles can be localized and the mask can be computed for each frame. The

center of the PSF has a Gaussian like shape; therefore, it can be localized precisely by simple Gaussian fitting. This localization can be shown to have an error that depends on the number of detected photons and reach accuracy of a few nanometers [19–22].

Multiplying each frame by the computed nanoparticles mask and applying time averaging, results in

$$R(x) = \int \left[\int s\left(x'\right) g(x', t) p(x - x') dx' \right] \widetilde{g}(x, t) dt, \tag{10.6}$$

where $\widetilde{g}(x, t)$ is the computed nanoparticle mask. Due to the random nature of the nanoparticle mask and the high localization accuracy we can assume that

$$\int g(x', t) \widetilde{g}(x, t) dt = \kappa + \delta(x' - x). \tag{10.7}$$

Using this in Eq. (10.6) results in

$$R(x) = s(x) p(0) + \kappa \int s(x') p(x - x') dx'. \tag{10.8}$$

The first term here is the high resolution object multiplied by a constant (the value of the PSF at the center) and the second term is the low resolution object obtained by the optical system. Since this term is the conventionally captured image, it can be subtracted from $R(x)$ to obtain $s(x)$.

10.4 Resolution Enhancement in Digital Holography

The principle presented in the previous Section 10.3 can be adapted to digital holography (DH) configuration [23]. The setup is presented in Fig. 10.4 (Plate 17), in which a Fourier plane hologram is recorded. In this setup the object is placed close to a pinhole, which serves as the reference beam that is required for the holography recording process.

We denote the high resolution object we would like to resolve by $s(x_1)$ and the random decoding pattern by $g(x_1, t)$. The pinhole is positioned in the Fourier domain hologram at a distance of Δx from the object $s(x_1)$. The detector captures the Fourier transform of the composed input field. Due to the nature of the CCD the result is multiplied by a rectangular function with a width of D. At the CCD plane we write the expression obtained at the CCD as:

$$I(x_2, t) = \left| \int \left(\delta(x - \Delta x) + s(x_1) g(x_1, t) \right) e^{-2\pi i x_1 x_2 / \lambda F} dx_1 \right|^2 rect\left(\frac{x_2}{D} \right). \tag{10.9}$$

This expression can be expended into three terms $I(x_2, t) = T_1(x_2, t) + T_2(x_2, t) + T_3(x_2, t)$ where

$$\begin{aligned}
T_1(x_2, t) &= \left(1 + \int s\left(x_1\right) g(x_1, t) e^{-2\pi i x_1 x_2 / \lambda F} dx_1 \right) rect\left(\frac{x_2}{D} \right). \\
T_2(x_2, t) &= \left(e^{-2\pi i \Delta x x_2 / \lambda F} \int s\left(x_1\right) g(x_1, t) e^{-2\pi i x_1 x_2 / \lambda F} dx_1 \right) rect\left(\frac{x_2}{D} \right) \\
T_3(x_2, t) &= \left(e^{2\pi i \Delta x x_2 / \lambda F} \int s^*\left(x_1\right) g^*(x_1, t) e^{2\pi i x_1 x_2 / \lambda F} dx_1 \right) rect\left(\frac{x_2}{D} \right)
\end{aligned} \tag{10.10}$$

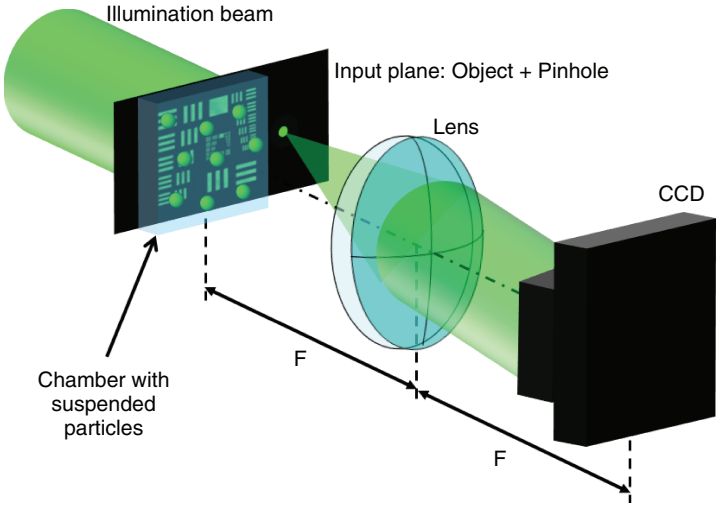

Figure 10.4 (Plate 17) Digital holography super-resolution setup. *Source*: Zalevsky Z., Gur E., Garcia J., Micó V., Javidi B. 2012. Figure 1. Reproduced with permission from The Optical Society. *See plate section for the color version*

The first step in the decoding is the inverse Fourier transform of $I(x_2, t)$, which results in a separation of the three terms in space. The T_1 term will appear on the optical axis and the T_2, T_3 terms will appear on the $+1$ and -1 orders due to the exponential term $e^{\pm 2\pi i \Delta x x_2/\lambda F}$. This separation allows us to take only the term we are interested in, that is, T_2. The inverse Fourier transform of T_2 can be written as:

$$I.F.T.\left\{T_2\left(x_2,t\right)\right\} = s\left(x_3-\Delta x\right) g\left(x_3-\Delta x,t\right) \otimes \left(D\sin c\left(\frac{x_3}{\lambda F}D\right)\right), \tag{10.11}$$

where $\otimes$ denotes convolution. The first two terms stem from the inverse Fourier transform of the Fourier transform of the object multiplied by the mask and the shift due to the delta function. The delta function is a result of the inverse Fourier transform of the exponential term before the integral in T_2. The last term is the Fourier transform of the *rect* function.

In the same manner as that presented in Section 10.3 we can calculate the decoding mask. We now multiply the resulting term by the decoding pattern and perform time averaging to obtain

$$R\left(x_3\right) = \int I.F.T\left\{T_2\left(x_3,t\right)\right\} g\left(x_3-\Delta x,t\right)dt. \tag{10.12}$$

By substituting (10.11) into (10.12) we have

$$R(x_3) = \int s(x_3-\Delta x)g(x_3-\Delta x,t) \otimes \left(D\sin c\left(\frac{x_3}{\lambda F}D\right)\right) g(x_3-\Delta x,t)dt. \tag{10.13}$$

We now look at the time-dependent terms in Eq. (10.13), which is the nanoparticles mask. Due to their small size of the nanoparticles and their random distribution we can write

$$\int g(x'-\Delta x,t)g(x_3-\Delta x,t)dt = \kappa + \delta(x'-x_3). \tag{10.14}$$

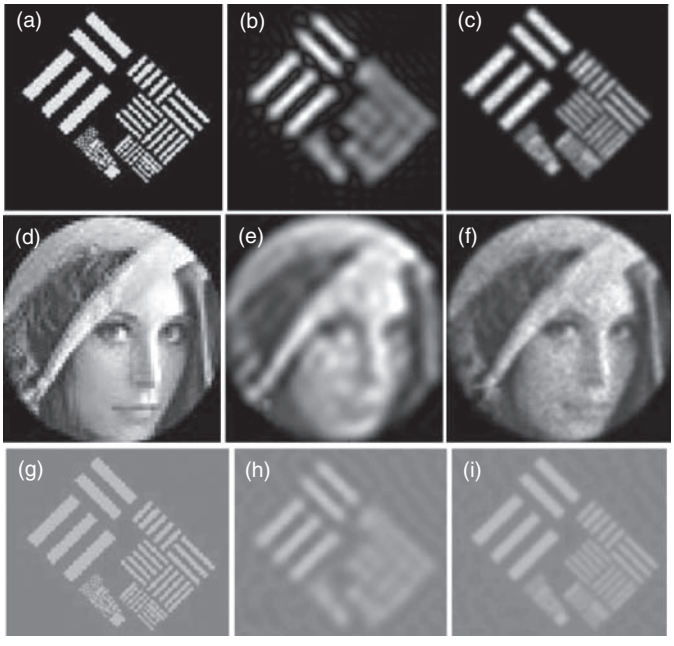

Figure 10.5 Numerical simulations for a binary amplitude resolution target (*top row*), Lena image (*middle row*), and phase resolution target (*bottom row*). The left column is the original high resolution object. The low resolution DH is in the center column and the super resolved object using metal nanoparticles is in the right column. *Source*: Zalevsky Z., Gur E., Garcia J., Micó V., Javidi B. 2012. Figure 2. Reproduced with permission from The Optical Society

We use the last equation to obtain the reconstruction

$$R(x_3) = D\kappa \int s(x' - \Delta x) \sin c \left(\frac{x_3 - x'}{\lambda F} D \right) dx' + \Delta x s(x_3 - \Delta x). \tag{10.15}$$

The first term here is the convolution from Eq. (10.13) and it corresponds to the low resolution image obtained by the convolution between the high resolution object and the *sinc* function caused by the finite size of the CCD. The second term is the term of interest to us and it is the high resolution reconstruction obtained by the proposed technique. Simulation results for the original object, the low resolution object and the super-resolution reconstruction are shown in Fig. 10.5.

10.5 Field of View Enhancement in Digital Holography

The resolution increase due to the placement of the nanoparticles in the object plane can be explained by considering the uncertainty principle of the Fourier transform. This principle states that

$$\Delta x \Delta f_x = const \tag{10.16}$$

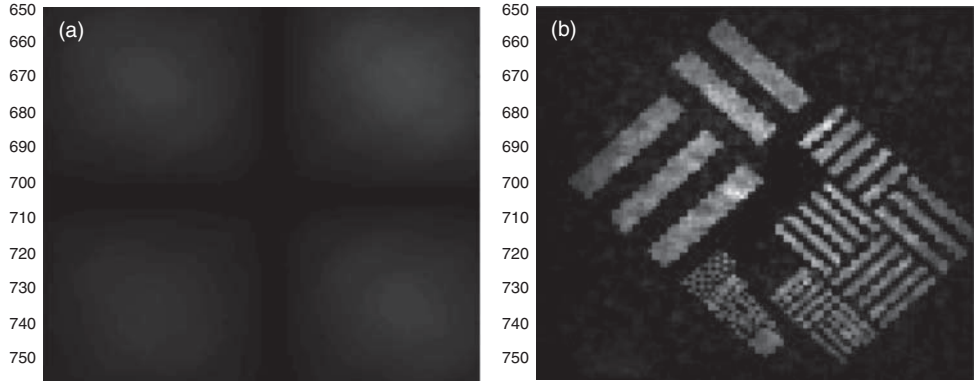

Figure 10.6 Numerical simulations for the FOV DH reconstruction. (a) The FOV reduced by a factor of 8. (b) Successful recovery of the original FOV with the nanoparticles' mask method. *Source*: Zalevsky Z., Gur E., Garcia J., Micó V., Javidi B. 2012. Figure 3. Reproduced with permission from The Optical Society

where x is the spatial coordinate and f_x is the spatial frequency. Δ designates the uncertainty or the range of values for each one of those two parameters. By using the metal nanoparticles in the object plane we limit our sampling of the object in each time frame to smaller Δx which now has the size of a metal nanoparticle; therefore, Δf_x increases; that is, more spatial frequencies can be recorded by the camera. Since, in the optical Fourier transform the frequency corresponds to real spatial coordinates, it means that in the Fourier plane we effectively need to increase the size of the CCD. Following this discussion, and remembering that up to multiplicative factors, the Fourier transform and Inverse Fourier transform are the same, if we reduce the sampling point in the CCD plane (the Fourier plane), we can obtain a larger FOV in the object plane. The finite size of the pixel on the CCD limits our ability to obtain large FOV, but using metal nanoparticles we can obtain sub-sampling in the CCD plane and thus larger FOV in the object plane.

In this case the term we are interested in, T_2 equals:

$$T_2(x_2) = \left[\left(e^{-2\pi i \Delta x x_2/\lambda F}\int s\left(x_1\right)e^{-2\pi i x_1 x_2/\lambda F}dx_1\right)g(x_2,t)\right] \otimes p(x_2). \tag{10.17}$$

Here $p(x_2)$ is the PSF that reduces the resolution of the recorded DH (the outcome of the finite sized pixels of the CCD). The decoding will include multiplication by high resolution pattern $g(x_2, t)$, inverse Fourier transform and time averaging:

$$R\left(x_3\right) = \int I.F.T\left\{T_2\left(x_2\right)g\left(x_3,t\right)\right\}dt, \tag{10.18}$$

thus

$$R\left(x_3\right) = \int \left[\left(s\left(x_3-\Delta x\right)\otimes G\left(\frac{x_3}{\lambda F},t\right)\right)P\left(\frac{x_3}{\lambda F},t\right)\right]\otimes G\left(\frac{x_3}{\lambda F},t\right)dt, \tag{10.19}$$

where G and P are the Fourier transforms of g and p respectively. Since

$$\int G\left(\frac{x'}{\lambda F},t\right)G\left(\frac{x_3-x_3{}'}{\lambda F},t\right)dt=\delta\left(x'-x_3-x_3{}'\right)+\kappa, \tag{10.20}$$

the result is

$$R\left(x_3\right)=s\left(x_3-\Delta x\right)\int P\left(\frac{x_3{}'}{\lambda F},t\right)dx_3'+\kappa\eta_s\eta_P, \tag{10.21}$$

where η_s,η_P are the averages of s and P respectively. The simulation results of this method are shown in Fig. 10.6.

10.6 Eliminating the DC Term and the Twin Images

A similar technique can be implemented in on-axis holographic scheme in order to eliminate the DC term and the twin image in the recorded hologram. Looking at the hologram with metal nanoparticles that are placed in proximity to the object, the time varying recorded frame can be written as

$$I\left(x,t\right)=\left|a\left(x\right)g\left(x,t\right)+A\right|^2, \tag{10.22}$$

where the reference is assumed to be a plane wave. Again, as before we capture multiple frames, localize the nanoparticles, and compute a decoding mask for each frame $\overline{g}(x,t)\approx g(x,t)$. Each frame is then digitally multiplied by the complex conjugate of the nanoparticles mask and time averaging of all frames is performed:

$$O\left(x\right)=\int I\left(x,t\right)\overline{g}^*\left(x,t\right)dt, \tag{10.23}$$

which can be written as

$$\begin{aligned}O\left(x\right)=&\int\left|A\right|^2\overline{g}^*\left(x,t\right)dt+\int\left|a\left(x\right)g\left(x,t\right)\right|^2\overline{g}^*\left(x,t\right)dt+\int A^*a\left(x\right)g\left(x,t\right)\overline{g}^*\left(x,t\right)dt\\&+\int Aa^*\left(x\right)g^*\left(x,t\right)\overline{g}^*\left(x,t\right)dt\end{aligned} \tag{10.24}$$

We now wish to eliminate all the terms but the third one which contains the actual imaged object. For this the nanoparticles should be chosen such that

$$g\left(x,t\right)=\exp\left(i\phi\left(x,y\right)\right), \tag{10.25}$$

where $\phi(x,t)$ can have one of four values: $\phi(x,t)=n\pi/2, n=0,1,2,3$. These four values can come from four different nanoparticle species. Since in the computed decoding mask we have to know not only the location of the nanoparticle, but also its phase, we can determine it by identifying to which of the four species the localized nanoparticle belongs. This can be accomplished by taking nanoparticles in different colors, shapes, scattering cross sections and so on. By considering Eq. (10.25), we observe that the third term in (10.24) equals

$$\int A^*a\left(x\right)g\left(x,t\right)\overline{g}^*\left(x,t\right)dt=\int A^*a\left(x\right)dt=\Delta TA^*a, \tag{10.26}$$

where ΔT is the integration time. Due to the random nature of the nanoparticles mask, and the phase values associated with each nanoparticle, the averaging of the other terms is zero, that is

$$\int \overline{g}^{*}(x,t)\,dt = \int g^{*}(x,t)\,\overline{g}^{*}(x,t)\,dt = \int |g(x,t)|^{2}\overline{g}^{*}(x,t)\,dt = 0. \tag{10.27}$$

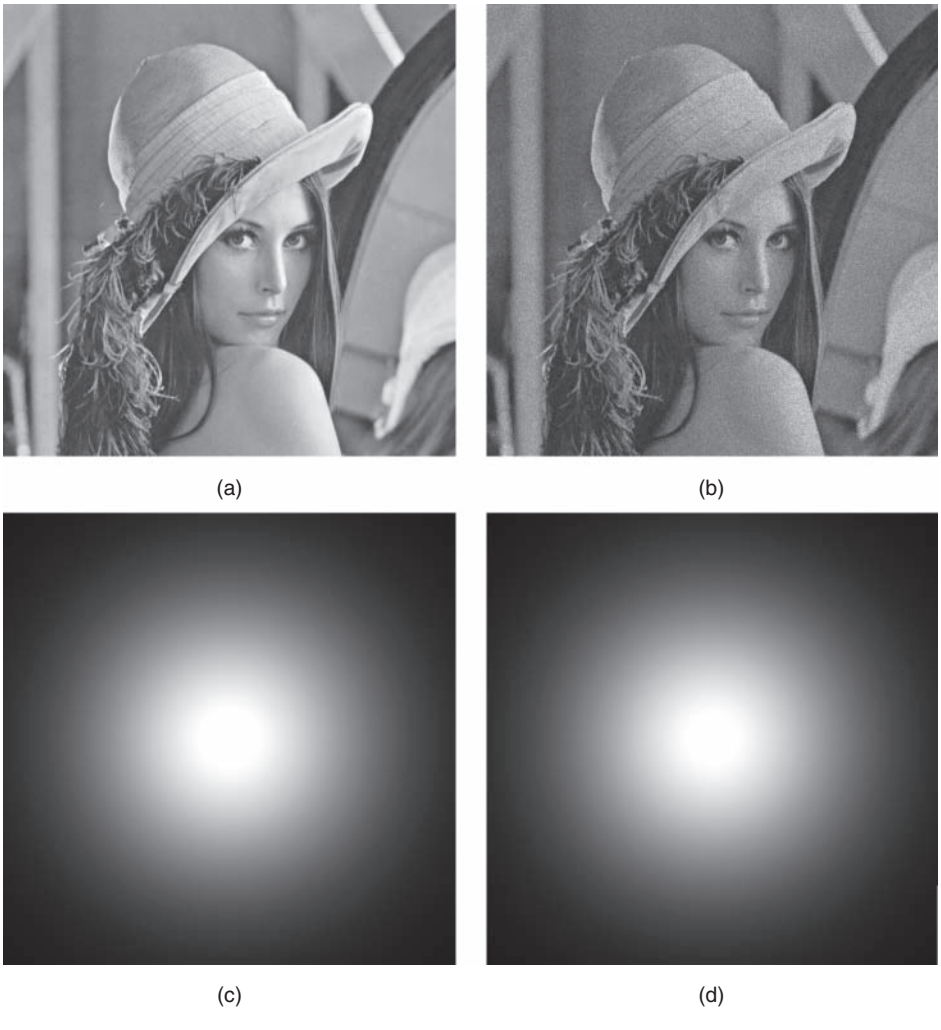

Figure 10.7 Simulation results for the reconstruction of amplitude and phase. The amplitude is a Lena image and the phase has a Gaussian profile. (a) Original field amplitude. (b) Reconstructed field amplitude. (c) Original field phase. (d) Reconstructed field phase. *Source*: Amihai Meiri, Eran Gur, Javier Garcia, Vicente Micó, Bahram Javidi, Zeev Zalevsky 2013. Reproduced with permission from SPIE

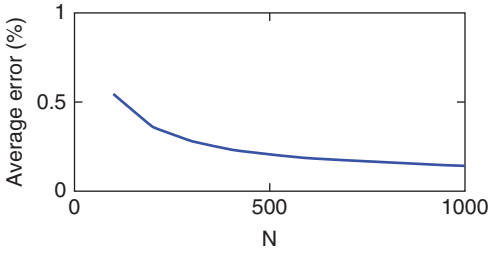

Figure 10.8 Phase error as a function of number of frames. *Source*: Amihai Meiri, Eran Gur, Javier Garcia, Vicente Micó, Bahram Javidi, Zeev Zalevsky 2013. Reproduced with permission from SPIE

Therefore we are left with

$$O(x) = \Delta T A^* a, \tag{10.28}$$

which is our imaged object, where the amplitude and phase are maintained. The simulated results for such a reconstruction are shown in Fig. 10.7 for 1000 recorded frames. The noise pattern of the reconstructed amplitude image in Fig. 10.7(a) is a result of this reconstruction and depends on the number of frames.

The relative error in phase reconstruction was calculated from the results of the simulations and shown on Fig. 10.8. This error was averaged over all pixels of the image and the results indicate that, even for a 100 frames, the error is as small as 0.5% and reduces rapidly with an increase in number of frames. This shows that using metal nanoparticles results in a very accurate reconstruction of the object phase.

10.7 Additional Applications

The random nanoparticle mask encoding can be used in other applications as well. As an example, we show the joint transform correlator (JTC) [24]. The JTC is a system that can be used to calculate the convolution of correlation between two functions in an all-optical setup. The setup for the JTC is presented in Fig. 10.9. A collimated beam is incident on two objects, h_1, h_2, which is located at the focal plane of lens L_1. At the back focal plane of the lens the recording medium is placed: see Fig. 10.9(a). In order to obtain the desired output (correlation of convolution between h_1 and h_2) we illuminate the recorded transparency by a collimated beam. The transparency is located at the focal plane of lens L_2 and the output is obtained at the back focal plane of the lens, see Fig. 10.9(b).

Using the metal nanoparticles random mask is depicted in Fig. 10.9(c). Here the nanoparticles are placed close to object h_1 and have the different phases as in Eq. (10.25). We now look at the intensity recorded by the transparency. The field at plane x_1 can be written as

$$U_1\left(x_1, t\right) = h_1\left(x_1 - X/2\right) g\left(x_1 - X/2, t\right) + h_2\left(x_1 + X/2\right), \tag{10.29}$$

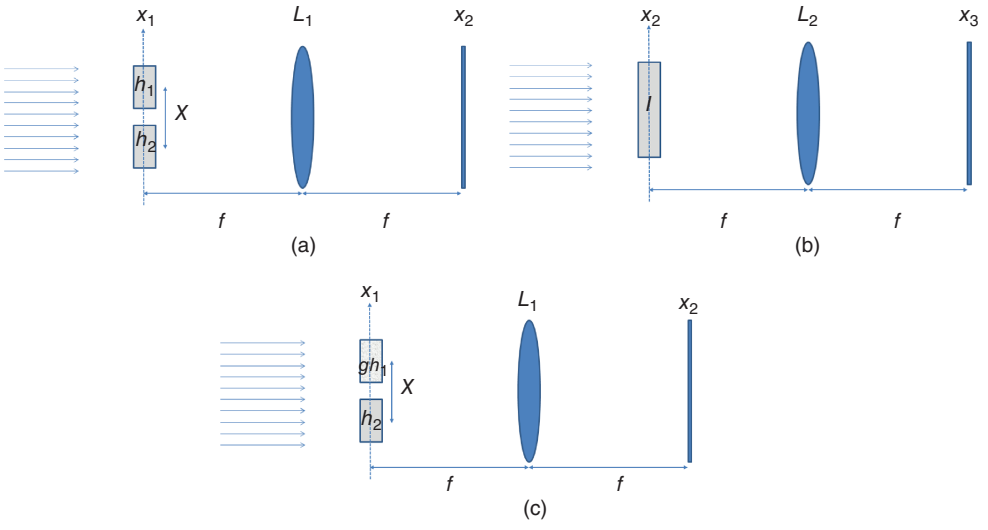

Figure 10.9 Joint transform correlator. (a) Recording the filter. (b) Obtaining the output

where g is the time varying nanoparticles phase encoding. In the rear focal plane of the lens L_1 we find the Fourier transform of the field

$$U_2\left(x_2,t\right)=\frac{1}{\lambda f}H_1\left(\frac{x_2}{\lambda f}\right)\otimes G\left(\frac{x_2}{\lambda f},t\right)e^{-j\pi x_2X/\lambda f}+\frac{1}{\lambda f}H_2\left(\frac{x_2}{\lambda f}\right)e^{j\pi x_2X/\lambda f}, \tag{10.30}$$

where $\otimes$ denotes convolution. Therefore, the intensity recorded by the transparency is:

$$\begin{aligned}I\left(x_2,t\right)=&\frac{1}{\lambda^2f^2}\left[\left|H_1\left(\tfrac{x_2}{\lambda f}\right)\otimes G\left(\tfrac{x_2}{\lambda f},t\right)\right|^2+\left|H_2\left(\frac{x_2}{\lambda f}\right)\right|^2\right]\\&+\frac{1}{\lambda^2f^2}\left[H_1\left(\frac{x_2}{\lambda f}\right)\otimes G\left(\frac{x_2}{\lambda f},t\right)H_2^*\left(\frac{x_2}{\lambda f}\right)e^{-j2\pi x_2X/\lambda f}\right]\\&+\frac{1}{\lambda^2f^2}\left[H_1^*\left(\frac{x_2}{\lambda f}\right)\otimes G^*\left(\frac{x_2}{\lambda f},t\right)H_2\left(\frac{x_2}{\lambda f}\right)e^{j2\pi x_2X/\lambda f}\right].\end{aligned} \tag{10.31}$$

We now compute the Fourier transform of the nanoparticle mask, multiply each frame by the corresponding computed mask, and perform time averaging:

$$\int I\left(x_2,t\right)G\left(\frac{x_2}{\lambda f},t\right)dt \tag{10.32}$$

The result is

$$I\left(x_2,t\right)=\frac{1}{\lambda^2f^2}\int\left[\left|H_1\left(\frac{x_2}{\lambda f}\right)\otimes G\left(\frac{x_2}{\lambda f},t\right)\right|^2+\left|H_2\left(\frac{x_2}{\lambda f}\right)\right|^2\right]G\left(\frac{x_2}{\lambda f},t\right)dt$$
$$+\frac{1}{\lambda^2f^2}\left[\int H_1\left(\frac{x_2}{\lambda f}\right)\otimes G\left(\frac{x_2}{\lambda f},t\right)H_2^*\left(\frac{x_2}{\lambda f}\right)e^{-j2\pi x_2X/\lambda f}G\left(\frac{x_2}{\lambda f},t\right)dt\right]$$
$$+\frac{1}{\lambda^2f^2}\left[\int H_1^*\left(\frac{x_2}{\lambda f}\right)\otimes G^*\left(\frac{x_2}{\lambda f},t\right)H_2\left(\frac{x_2}{\lambda f}\right)e^{j2\pi x_2X/\lambda f}G\left(\frac{x_2}{\lambda f},t\right)dt\right] \quad (10.33)$$

We look at the time integrals and obtain that:

$$\int\left|H_1\left(\frac{x_2}{\lambda f}\right)\otimes G\left(\frac{x_2}{\lambda f},t\right)\right|^2G\left(\frac{x_2}{\lambda f},t\right)dt=0$$
$$\int\left|H_2\left(\frac{x_2}{\lambda f}\right)\right|^2G\left(\frac{x_2}{\lambda f},t\right)dt=0$$
$$\int G\left(\frac{x_2}{\lambda f},t\right)G\left(\frac{x_2}{\lambda f},t\right)dt=0$$
$$\int G^*\left(\frac{x_2}{\lambda f},t\right)G\left(\frac{x_2}{\lambda f},t\right)dt=const \quad (10.34)$$

as in the first three integrals of (10.34) there is a remaining time varying phase, which is averaged to zero while only in forth integral the time varying phase term is cancelled. The calculation of the nanoparticle mask is performed in the same way as in Section 10.6: we have four nanoparticle species, with different phases $\phi(x,t)=n\pi/2, n=0,1,2,3$. The nanoparticle mask equals

$$g\left(x,t\right)=\exp\left(i\phi\left(x,y\right)\right). \quad (10.35)$$

We can now localize each nanoparticle and identify its associated phase by identifying the species. Therefore

$$\int I\left(x_2,t\right)G\left(\frac{x_2}{\lambda f},t\right)dt=\frac{1}{\lambda^2f^2}H_1^*\left(\frac{x_2}{\lambda f}\right)H_2\left(\frac{x_2}{\lambda f}\right)e^{j2\pi x_2X/\lambda f}. \quad (10.36)$$

When illuminating the transparency as in Fig. 10.9(b) the field at the output is the Fourier transform of Eq. (10.36) and can now be expressed as

$$U_3\left(x_3\right)=\frac{1}{\lambda f}\left[h_1^*\left(-x_3\right)\otimes h_2\left(x_3\right)\otimes\delta\left(x_3+X\right)\right]. \quad (10.37)$$

The result is the cross correlation of objects h_1 and h_2 shifted in space by X.

References

[1] Gabor D., "A New Microscopic Principle," *Nature* **161**, 777–778 (1948).

[2] Goodman J. W., *Introduction to Fourier Optics* (Roberts and Company Publishers, 2005).

[3] Leith E. N. and J. Upatnieks, "Reconstructed wavefronts and communication theory," *JOSA* **52**, 1123–1128 (1962).

[4] Liu G. and P. D. Scott, "Phase retrieval and twin-image elimination for in-line Fresnel holograms," *JOSA A* **4**, 159–165 (1987).

[5] Onural L. and P. D. Scott, "Digital decoding of in-line holograms," *Optical Engineering* **26**, 261124–261124 (1987).

[6] Zhang Y. and X. Zhang, "Reconstruction of a complex object from two in-line holograms," *Optics Express* **11**, 572–578 (2003).

[7] Jain P. K., K. S. Lee, I. H. El-Sayed, and M. A. El-Sayed, "Calculated absorption and scattering properties of gold nanoparticles of different size, shape, and composition: applications in biological imaging and biomedicine," *The Journal of Physical Chemistry B* **110**, 7238–7248 (2006).

[8] Brioude A., X. C. Jiang, and M. P. Pileni, "Optical properties of gold nanorods: DDA simulations supported by experiments," *J. Phys. Chem. B* **109**, 13138–13142 (2005).

[9] Susie E. and A. El-Sayed Mostafa, "Why gold nanoparticles are more precious than pretty gold: Noble metal surface plasmon resonance and its enhancement of the radiative and nonradiative properties of nanocrystals of different shapes," *Chemical Society Reviews* **35**, 209–217 (2006).

[10] Link S., M. B. Mohamed, and M. A. El-Sayed, "Simulation of the optical absorption spectra of gold nanorods as a function of their aspect ratio and the effect of the medium dielectric constant," *The Journal of Physical Chemistry B* **103**, 3073–3077 (1999).

[11] Kelly K. L., E. Coronado, L. L. Zhao, and G. C. Schatz, "The optical properties of metal nanoparticles: the influence of size, shape, and dielectric environment," *J. Phys. Chem. B* **107**, 668–677 (2003).

[12] Su K. H., Q. H. Wei, X. Zhang, J. J. Mock, D. R. Smith, and S. Schultz, "Interparticle coupling effects on plasmon resonances of nanogold particles," *Nano Letters* **3**, 1087–1090 (2003).

[13] Jain P. K., W. Huang, and M. A. El-Sayed, "On the universal scaling behavior of the distance decay of plasmon coupling in metal nanoparticle pairs: a plasmon ruler equation," *Nano Letters* **7**, 2080–2088 (2007).

[14] Browning L. M., T. Huang, and X. N. Xu, "Far-field photostable optical nanoscopy (PHOTON) for real-time super-resolution single-molecular imaging of signaling pathways of single live cells," *Nanoscale* **4**, 2797 (2012).

[15] Valeur B., *Molecular Fluorescence: Principles and Applications* (VCH Verlagsgesellschaft Mbh, 2002).

[16] Diaspro A., *Nanoscopy and Multidimensional Optical Fluorescence Microscopy* (Chapman & Hall, 2009).

[17] Gur A., D. Fixler, V. Micó, J. Garcia, and Z. Zalevsky, "Linear optics based nanoscopy," *Optics Express* **18**, 22222–22231 (2010).

[18] Inouye Y. and S. Kawata, "Near-field scanning optical microscope with a metallic probe tip," *Optics Letters* **19**, 159–161 (1994).

[19] Andersson S. B., "Precise localization of fluorescent probes without numerical fitting," in *4th IEEE International Symposium on Biomedical Imaging: From Nano to Macro, 2007. ISBI 2007* (IEEE, 2007), pp. 252–255.

[20] Cheezum M. K., W. F. Walker, and W. H. Guilford, "Quantitative Comparison of Algorithms for Tracking Single Fluorescent Particles," *Biophysical Journal* **81**, 2378–2388 (2001).

[21] Carter B. C., G. T. Shubeita, and S. P. Gross, "Tracking single particles: a user-friendly quantitative evaluation," *Physical Biology* **2**, 60 (2005).

[22] Pertsinidis A., Y. Zhang, and S. Chu, "Subnanometre single-molecule localization, registration and distance measurements," *Nature* **466**, 647–651 (2010).
[23] Zalevsky Z., E. Gur, J. Garcia, V. Micó, and B. Javidi, "Superresolved and field-of-view extended digital holography with particle encoding," *Optics Letters* **37**, 2766–2768 (2012).
[24] Weaver C. S. and J. W. Goodman, "A technique for optically convolving two functions," *Applied Optics* **5**, 1248 (1966).